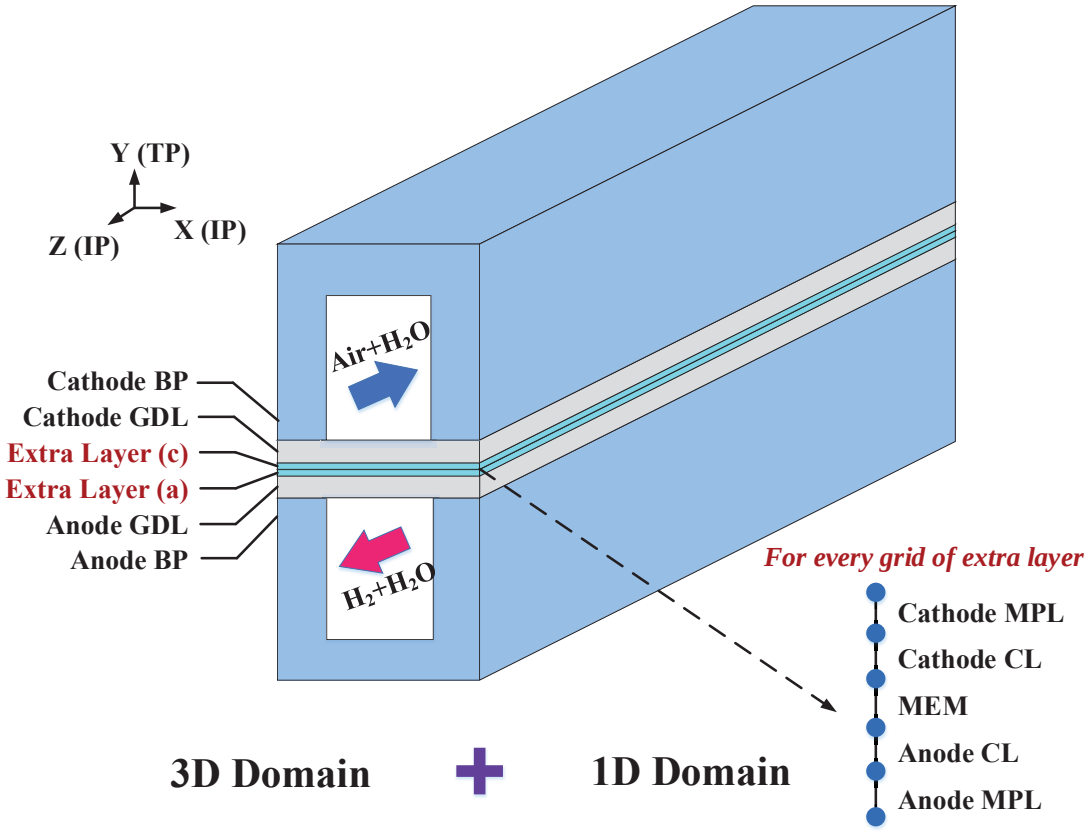

Fig. 1. Computational domain of the "3D+1D" model including the 3D domain (with geometry) and the 1D domain (no geometry).

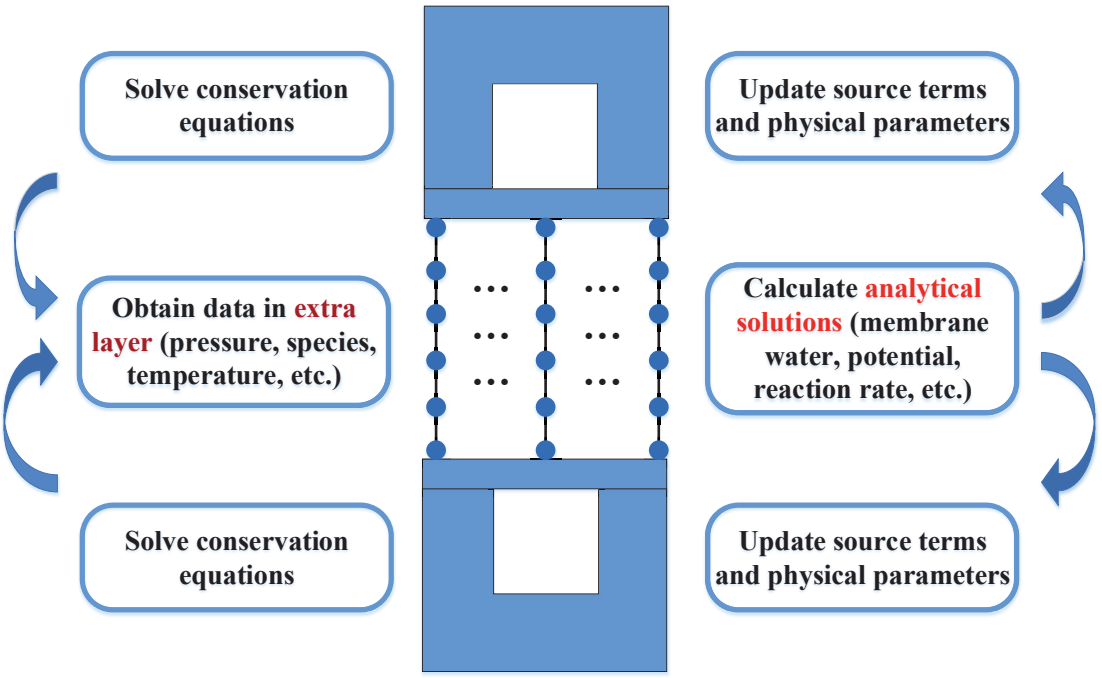

Fig. 2. Solution flowchart of the “3D+1D” model in every iteration.

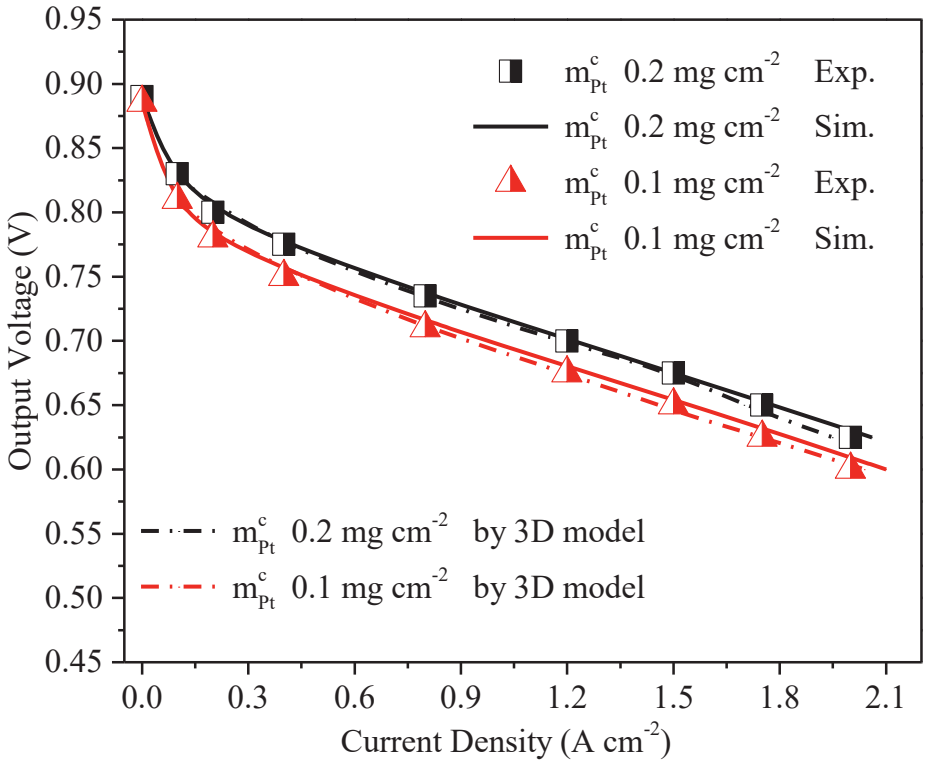

Fig. 3. Comparison between simulated polarization curves by the "3D+1D" model and experimental data under two cathode Pt loadings [27]. The preceding simulation results of 3D model [26] are also given. Operating conditions (anode/cathode): inlet relative humidity (1.0/1.0), stoichiometric ratio (3.0/4.0), back total pressure (1.5/1.5 atm), operating temperature (353.15 K).

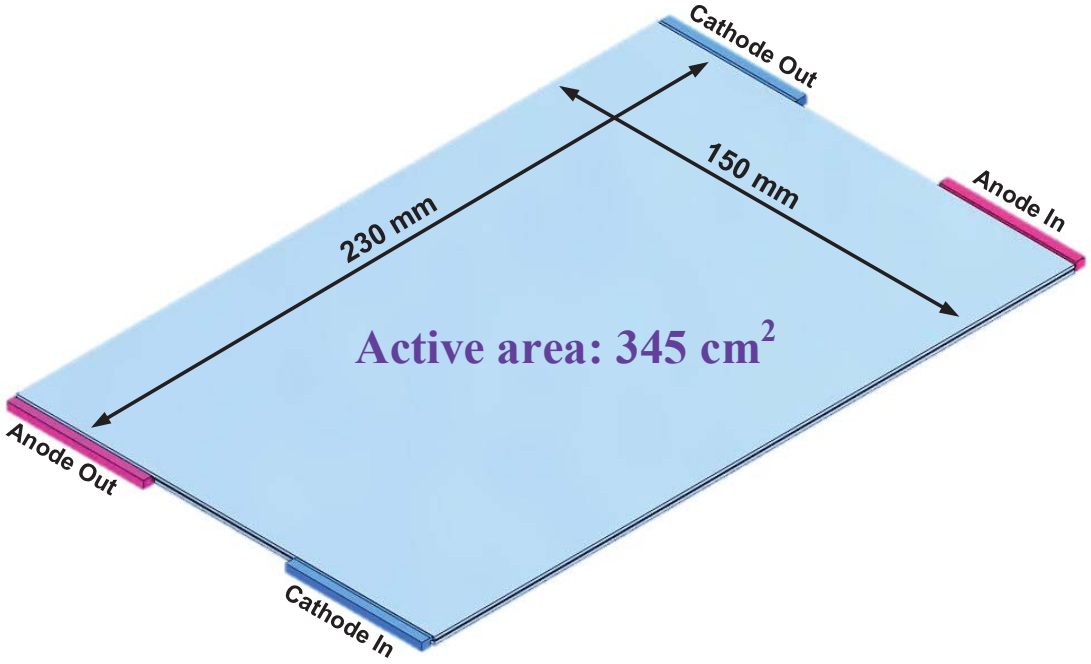

Fig. 4. Schematic of the large-scale computational domain with 345 cm^2 active area.

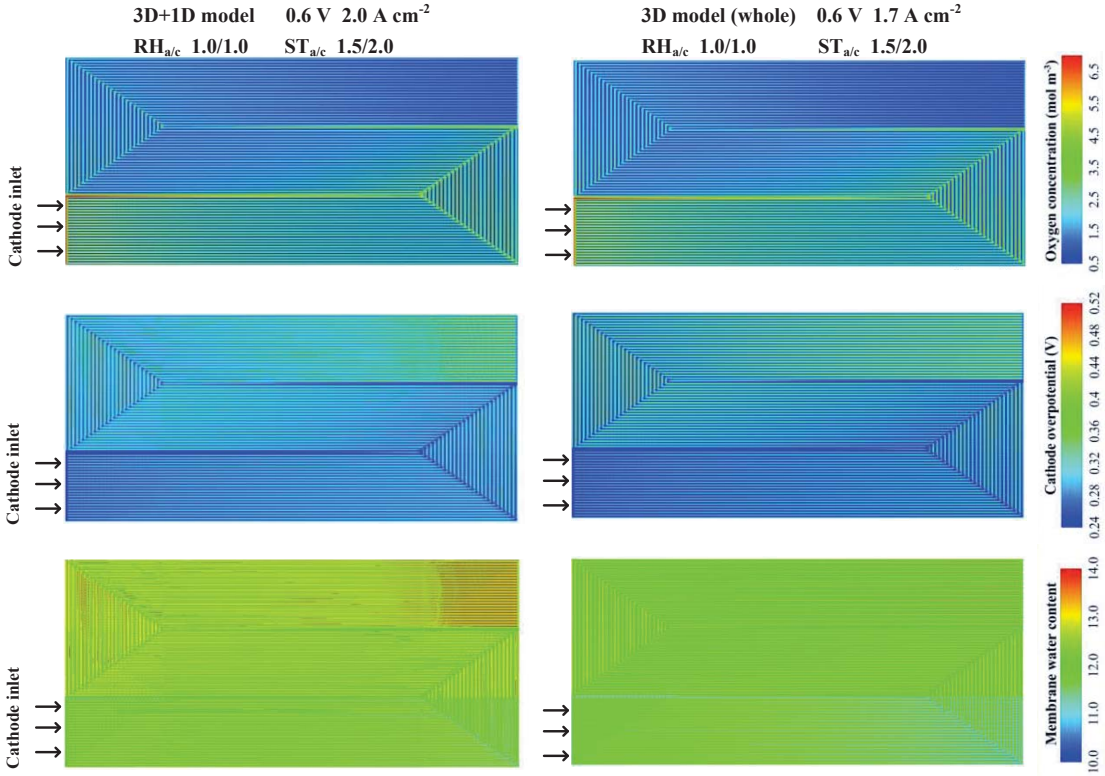

Fig. 5. Comparison of oxygen molar concentration, cathode electrochemical overpotential and membrane water content between the 3D model and the "3D+1D" model at the 0.6 V output voltage data point.

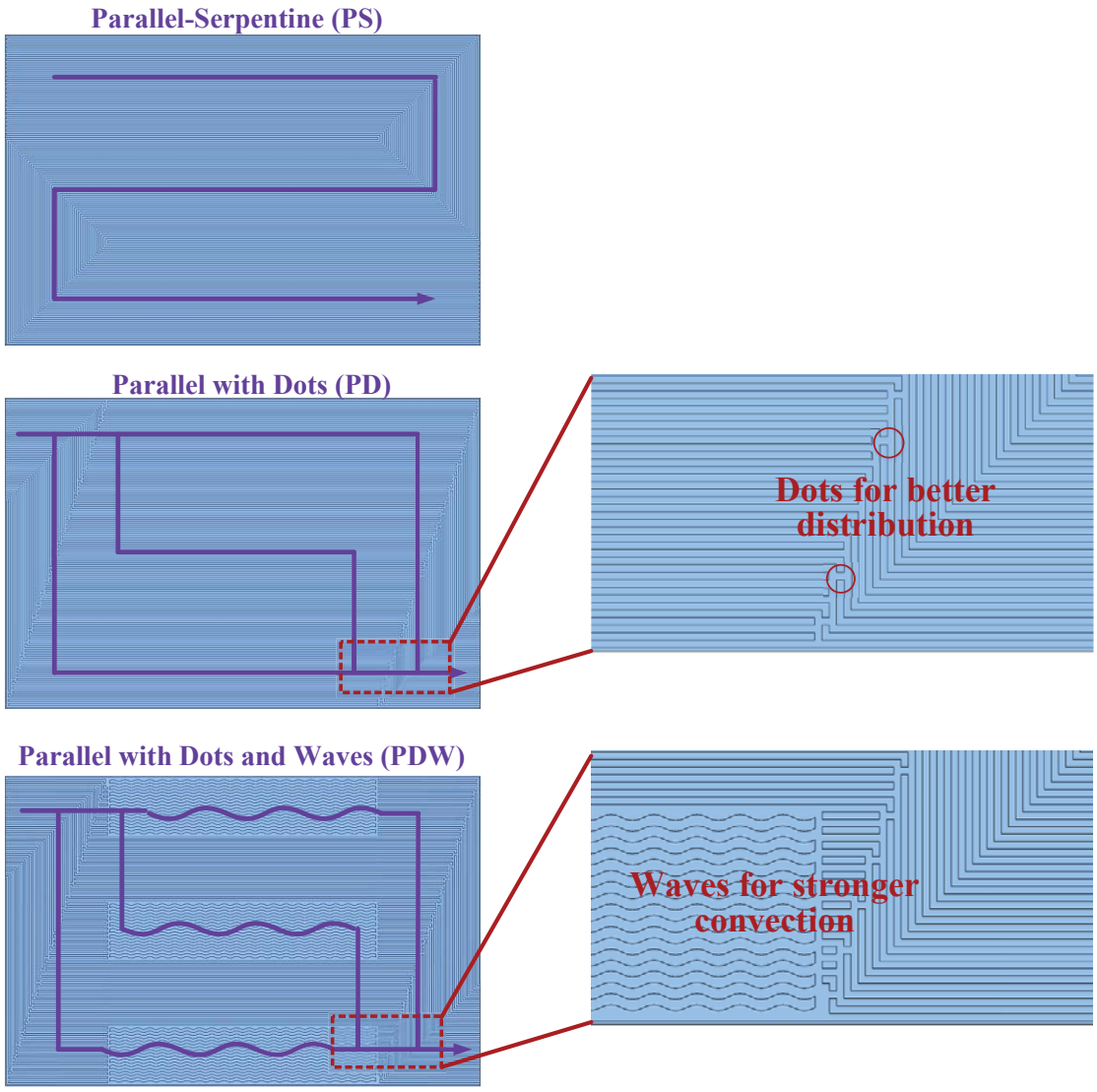

Fig. 6. Schematic of the three different flow field designs (PS, PD, PDW).

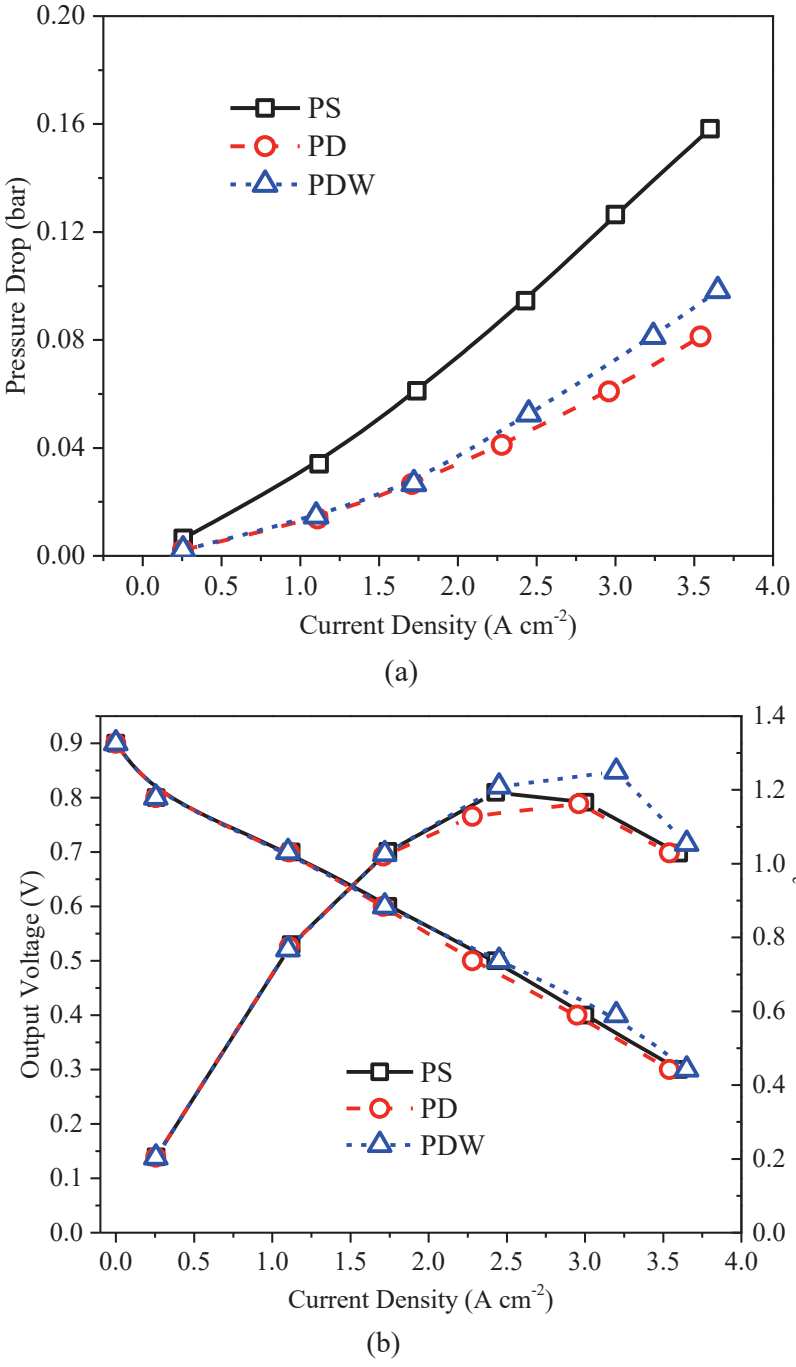

Fig. 7. Comparison of (a) pressure drop; (b) polarization curve and net power density among the three cathode flow field designs under high inlet humidity ($RH_{a/c}$ 1.0/1.0) and stoichiometric ratio ($ST_{a/c}$ 1.5/2.0).

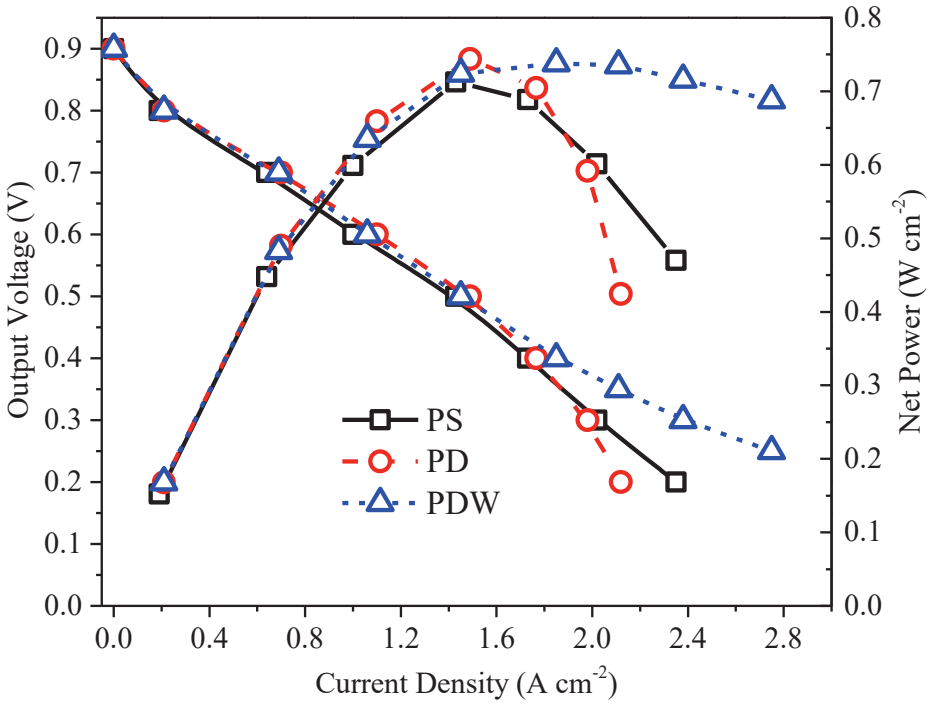

Fig. 8. Comparison of polarization curve and net power density among the three cathode flow field designs under low inlet humidity ($RH_{a/c}$ 0.4/0.2) and stoichiometric ratio ($ST_{a/c}$ 1.2/1.6).

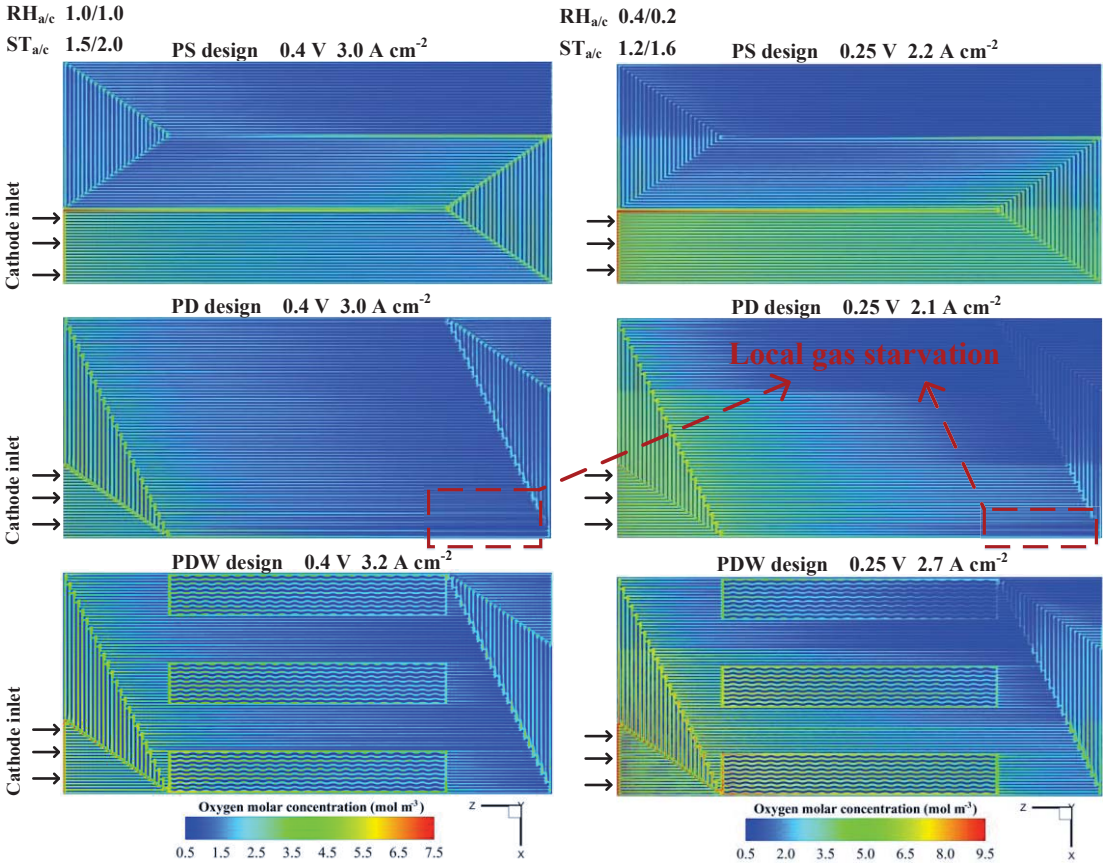
RH$_{a/c}$ 1.0/1.0
ST$_{a/c}$ 1.5/2.0
PS design 0.4 V 3.0 A cm^{-2}
RH$_{a/c}$ 0.4/0.2
ST$_{a/c}$ 1.2/1.6
PS design 0.25 V 2.2 A cm^{-2}
Cathode inlet
PD design 0.4 V 3.0 A cm^{-2}
PD design 0.25 V 2.1 A cm^{-2}
Local gas starvation
Cathode inlet
PDW design 0.4 V 3.2 A cm^{-2}
PDW design 0.25 V 2.7 A cm^{-2}
Cathode inlet
Oxygen molar concentration (mol m^3)
0.5 1.5 2.5 3.5 4.5 5.5 6.5 7.5
z
x
Oxygen molar concentration (mol m^3)
0.5 2.0 3.5 5.0 6.5 8.0 9.5
z
x

(a)

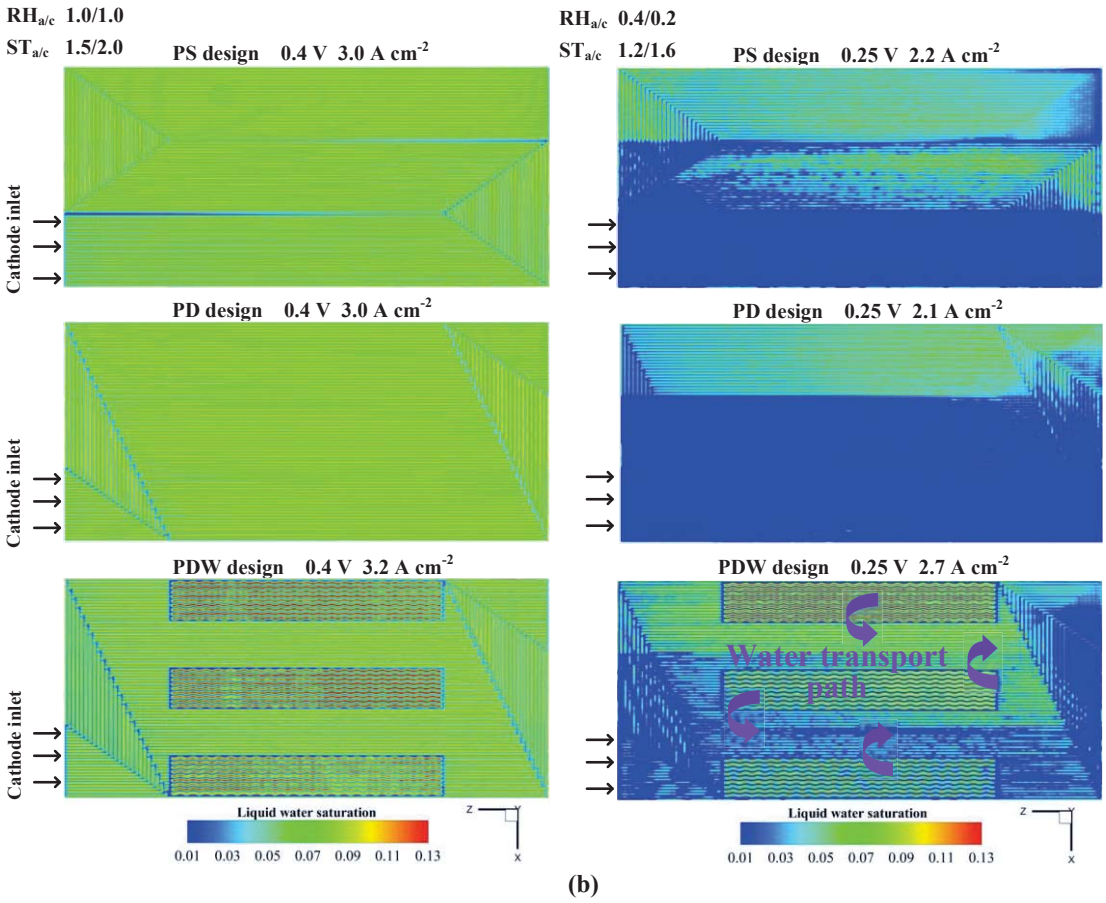

Fig. 9. Comparison of (a) oxygen molar concentration contours; (b) liquid water saturation contours in the middle plane of cathode GDL among the three flow field designs under different inlet conditions.

Table 1. Source terms of 3D sub-model.

Source terms		Unit
$S_{\mathrm{m}}=\begin{cases}-S_{\mathrm{v\text{-}l}}+\frac{J_{\mathrm{vp}}}{\delta_{\mathrm{EL}}}M_{\mathrm{H_2O}}+\frac{J_{\mathrm{H_2}}}{\delta_{\mathrm{EL}}}M_{\mathrm{H_2}} & \text{AEL}\\ -S_{\mathrm{v-l}}+\frac{J_{\mathrm{vp}}}{\delta_{\mathrm{EL}}}M_{\mathrm{H_2O}}+\frac{J_{\mathrm{O_2}}}{\delta_{\mathrm{EL}}}M_{\mathrm{O_2}} & \text{CEL}\\ -S_{\mathrm{v-l}} & \text{GDLs, GCHs}\end{cases}$		kg m^{-3} s^{-1}
$S_{\mathrm{u}}=-\frac{\mu_g}{Kk_g}\vec{u}_g$	GDLs, ELs	kg m^{-2} s^{-2}
$S_{\mathrm{H_2}}=\frac{J_{\mathrm{H_2}}}{\delta_{\mathrm{EL}}}M_{\mathrm{H_2}}$	AEL	kg m^{-3} s^{-1}
$S_{\mathrm{O_2}}=\frac{J_{\mathrm{O_2}}}{\delta_{\mathrm{EL}}}M_{\mathrm{O_2}}$	CEL	kg m^{-3} s^{-1}
$S_{\mathrm{vp}}=\begin{cases}-S_{\mathrm{v\text{-}l}}+\frac{J_{\mathrm{vp}}}{\delta_{\mathrm{EL}}}M_{\mathrm{H_2O}} & \text{AEL}\\ -S_{\mathrm{v-l}}+\frac{J_{\mathrm{vp}}}{\delta_{\mathrm{EL}}}M_{\mathrm{H_2O}} & \text{CEL}\\ -S_{\mathrm{v-l}} & \text{GDLs, GCHs}\end{cases}$		kg m^{-3} s^{-1}
$S_{\mathrm{T}}=\begin{cases}hS_{\mathrm{v\text{-}l}}+\frac{J_{\mathrm{T}}}{\delta_{\mathrm{EL}}} & \text{AEL}\\ hS_{\mathrm{v\text{-}l}}+\frac{J_{\mathrm{T}}}{\delta_{\mathrm{EL}}} & \text{CEL}\\ hS_{\mathrm{v\text{-}l}}+\left\|\nabla\varphi_{\mathrm{ele}}\right\|^2\kappa_{\mathrm{ele}}^{\mathrm{eff}} & \text{GDLs}\\ \left\|\nabla\varphi_{\mathrm{ele}}\right\|^2\kappa_{\mathrm{ele}}^{\mathrm{eff}} & \text{BPs}\\ hS_{\mathrm{v\text{-}l}} & \text{GCHs}\end{cases}$		W m^{-3}
$S_{\mathrm{lw}}=\begin{cases}S_{\mathrm{v-l}}+\frac{J_{\mathrm{lw}}}{\delta_{\mathrm{EL}}}M_{\mathrm{H_2O}} & \text{ELs}\\ S_{\mathrm{v-l}} & \text{GDLs}\end{cases}$		
$S_{\mathrm{lw}}=S_{\mathrm{v-l}}-\rho_{\mathrm{lw}}\frac{K_{\mathrm{through}}k_{\mathrm{lw}}}{\mu_{\mathrm{lw}}\delta_{\mathrm{mesh}}}\nabla P_{\mathrm{lw}}^{\mathrm{GDL}}$	GCHs [25]	kg m^{-3} s^{-1}
$S_{\mathrm{ele}}=\frac{J_{\mathrm{ele}}}{\delta_{\mathrm{EL}}}$	ELs	A m^{-3}

$$S_{\text{v-l}} = \begin{cases} \gamma_{\text{v-l}} \varepsilon (1-s)(C_{\text{vp}} - C_{\text{sat}}) M_{\text{H}_2\text{O}} & C_{\text{vp}} > C_{\text{sat}} \\ \gamma_{\text{v-l}} \varepsilon s (C_{\text{vp}} - C_{\text{sat}}) M_{\text{H}_2\text{O}} & C_{\text{vp}} < C_{\text{sat}} \end{cases} \qquad \text{kg m}^{-3}\ \text{s}^{-1}$$

Table 2. Values and expressions of model parameters.

Parameters	Symbol	Values or expressions
Dry ionomer density (kg m^{-3})	ρ_{im}	1980
Equivalent weight of dry ionomer (kg mol^{-1})	EW	1.1
Porosity of porous electrodes	ε_{GDL}, ε_{MPL}	0.6, 0.5
Volume fraction of platinum/carbon catalyst [26]	$\varepsilon_{pt/c}$	$\frac{m_{pt}}{\delta_{CL}}\left[\frac{1}{\rho_{pt}}+\left(\frac{1}{\zeta_{pt/c}}-1\right)\frac{1}{\rho_c}\right]$
Volume fraction of ionomer [26]	ε_{im}	$\frac{\zeta_{im/c} m_{pt}}{\delta_{CL}\rho_{im}}\left(\frac{1}{\zeta_{pt/c}}-1\right)\left(1+\frac{M_{lw}\rho_{im}}{\rho_{lw}EW}\lambda\right)$
Porosity of porous electrodes	ε_{CL}	$1-\varepsilon_{pt/c}-\varepsilon_{im}$
Gas bulk diffusivity (m^2 s^{-1})	D_{H_2}, D_{O_2}, $D^a_{H_2O}$, $D^c_{H_2O}$	$1.005\times10^{-4}(\frac{T}{333.15})^{1.5}(\frac{101325}{P})$ $2.652\times10^{-4}(\frac{T}{333.15})^{1.5}(\frac{101325}{P})$ $1.005\times10^{-4}(\frac{T}{333.15})^{1.5}(\frac{101325}{P})$ $2.982\times10^{-4}(\frac{T}{333.15})^{1.5}(\frac{101325}{P})$
Intrinsic permeability (m^2)	K_{GDL}, K_{MPL}, K_{CL}, K_{MEM}, K_{MF}	2.0e-12, 1.0e-12, 1.0e-13, 2.0e-20, 1.0e-9
Relative permeability	k_{lw}, k_g	$s^{3.0}$, $(1.0-s)^{3.0}$
EOD coefficient	n_d	$2.5\lambda/22.0$
Electronic conductivity (S m^{-1})	$\kappa_{ele,BP}$, $\kappa_{ele,GDL}$, $\kappa_{ele,MPL}$, $\kappa_{ele,CL}$	20000, 8000, 5000, 5000
Bruggmann correction	D_i^{eff}	$D_i\,\varepsilon^{1.5}$
Phase change rate (s^{-1})	γ_{vl}, γ_{vm}	100, 1.3
Entropy change (J mol^{-1} K^{-1})	ΔS_a, ΔS_c	270.6, -178.7

Electrochemical active surface area ($m^2\ g^{-1}$)	a_{ECSA}	70
Reference exchange current density ($A\ m^{-2}$)	$i_{0,a}^{ref}$, $i_{0,c}^{ref}$	3.5, 3.5e-4
Reference concentration ($mol\ m^{-3}$)	$C_{O_2}^{ref}$, $C_{O_2}^{ref}$	56.4, 3.39
Transfer coefficient	α_a, α_c	0.5, 0.5

Table 3. Grid independency test results.

Mesh	Grid quantity	Max size(mm)		Current density($A\ cm^{-2}$)
		In-plane	Through-plane	
1	14,000	1.0	0.2	1.9532
2	27,000	1.0	0.1	2.0410
3	17,500	0.8	0.2	1.9516
4	33,750	0.8	0.1	2.0410
5	28,000	0.5	0.2	1.9529
6	54,000	0.5	0.1	2.0410
7	60,800	1.0	0.07	2.0708
8	100,000	1.0	0.05	2.0855

Table 4. Mesh quantity and simulation time of the comparison cases.

Computational domain	Mesh quantity		Simulation time (h)	
	3D+1D	whole 3D	3D+1D	whole 3D
Single-channel	60,800	216,000	0.03	0.5
345 cm^2 cell	7,425,095	18,191,970	~3	~60
Hardware configuration	CPU: Intel(R) Xeon(R) Gold 6310 @ 2.10GHz Memory: 256G			

Table 5. Geometry information of the computational domains.

Parameters	Values (Single-channel/345 cm^2 cell)
Channel width (mm)	0.5/1.0
Channel height (mm)	0.7/1.0
Channel length (mm)	100/230
Channel number	1/75
Land width (mm)	0.5/1.0
BP height (mm)	1.0/NA
Wave number (PDW design)	3×10
Wave width (mm)	1.5
MEA layer thickness, $\delta_{GDL}, \delta_{MPL}, \delta_{ACL}, \delta_{MEM}, \delta_{CCL}$ (μm)	180, 20, 3 ,18, 10
Extra layer thickness, δ_{EL} (μm)	20

Highlights

- A “3D+1D” modeling approach for large-scale simulation is proposed.
- The model gains excellent calculation efficiency with decent accuracy.
- Simulation time can be shortened by 20 folds compared with 3D model.
- The partitioning optimization design of flow field is tested.
- Parallel flow field with dots and waves show good performance and adaptability.

“3D+1D” modeling approach toward large-scale PEM fuel cell simulation and partitioned optimization study on flow field

Biao Xie[1], Guobin Zhang[1], Yang Jiang[2], Renfang Wang[3], Xia Sheng[4], Fuqiang Xi[5], Ziliang Zhao[4], Wenmiao Chen[5], Ying Zhu[3], Yao Wang[3], Huizhi Wang[2], Kui Jiao[1]*

1. State Key Laboratory of Engines, Tianjin University, 135 Yaguan Rd, Tianjin, China, 300350

2. Department of Mechanical Engineering, Imperial College London, Exhibition Road, South Kensington Campus, London, United Kingdom, SW7 2AZ

3. Shanghai Hydrogen Propulsion Technology Co. Ltd., Innovation Park, Antuo Road, Jiading, Shanghai, China, 201804

4. New Energy Development Inst, China FAW Group Co., Ltd, 1 Xinhongqi Street, Changchun, China, 130013

5. Weichai Power Co. Ltd., 197A Fushou St. E., Weifang, China, 261016

*Corresponding author: kjiao@tju.edu.cn; tel: +86-22-27404460; fax +86-22-27383362

Abstract

A “3D+1D” PEM fuel cell model is developed in order to implement large-scale simulation with enhanced calculation efficiency. The model consists of the three-dimensional (3D) part and the one-dimensional (1D) part, which are related by adding two extra layers in the middle of the 3D computational domain. Bipolar plate (BP), gas channel (GCH) and gas diffusion layer (GDL) along with the extra layer (EL) form the 3D computational domain. Other components, micro-porous layer (MPL), catalyst layer (CL) and membrane (MEM) are treated as 1D computational domain and integrated into the grids of extra layer. The 3D sub-model solves conservation equations and provides scalar data for the 1D sub-model to obtain solutions of flux equations, in

turn updating parameters of the 3D domain to proceed iterations. The “3D+1D” model considers the strongly-coupled physicochemical phenomena comprehensively inside PEM fuel cell including mass transfer (reactant gas and liquid water), electrochemical reaction, membrane water balance and heat transfer. The trade-off between model accuracy and calculation efficiency is evaluated with detail by comparing the simulation results and time cost of the “3D+1D” model with those of the whole 3D model. The calculation speed is found to be greatly boosted via the “3D+1D” approach and acceptable accuracy is obtained at the same time. Specifically, the simulation time can be shortened by 20 folds for the large-scale case in this study. Then, three flow field designs are compared on a 345 cm^2 PEM fuel cell domain using the proposed “3D+1D” model, namely the parallel-serpentine design (PS design), the parallel design with dots in the distribution zone (PD design) and the parallel design with dots in the distribution zone and waves in straight-flow zone (PDW design). Owing to the addition of wavy structure, the PDW design gives excellent performance under high current density with low external humidification and stoichiometric ratio due to enhanced gas convection and self-humidification effect. This proves the feasibility and potential of partitioned optimization design on PEM fuel cell flow field, meanwhile emphasizing the suitability of the “3D+1D” modeling approach for occasions where the full morphology of flow field layout should be considered.

Keywords

PEM fuel cell; Large-scale simulation; “3D+1D” approach; Flow field; Partitioned optimization design

Nomenclature

A	specific surface area (m^{-1})
A_{act}	active area (m^2)
a	water activity
a_{ECSA}	electrochemical active surface area ($m^2\ g^{-1}$)
C_i	gas molar concentration ($mol\ m^{-3}$)
C_p	specific heat capacity ($J\ mol^{-1}\ K^{-1}$)
D_i	gas diffusivity ($m^2\ s^{-1}$)
E_{rev}	reversible voltage (V)
EW	equivalent weight of ionomer ($kg\ mol^{-1}$)
F	faraday’s constant ($C\ mol^{-1}$)
H	henry’s constant ($Pa\ m^3\ mol^{-1}$)
h	latent heat of water ($J\ mol^{-1}$)
i_0^{ref}	reference exchange current density ($A\ m^{-2}$)
J	flux ($mol\ m^{-2}\ s^{-1}$ or $W\ m^{-2}$)
j	electrochemical reaction rate in current form ($A\ m^{-3}$)
K	intrinsic permeability (m^2)

k	relative permeability
k^{eff}	effective thermal conductivity (W m^{-1} K^{-1})
k_{elch}	collection of electrochemical parameters (A m^{-3})
M	molar mass (kg mol^{-1})
m	specific mass (kg m^{-2})
$\dot{m}$	mass flux (kg m^{-2} s^{-1})
n_{d}	electro-osmotic drag coefficient
P	pressure (Pa)
R	universal gas constant (J mol^{-1} K^{-1})
R_{local}	local transport resistance (s m^{-1})
RH	relative humidity
S	source term (kg m^{-3} s^{-1} ,W m^{-3} …)
ST	stoichiometric ratio
ΔS	entropy change (J mol^{-1} K^{-1})
s	liquid water saturation
T	temperature (K)
$\vec{u}$	superficial velocity vector (m s^{-1})
V_{out}	output voltage (V)
W	power density (W cm^{-2})
X	Mole fraction

Y_i	gas species mass fraction

Greek letters

α	transfer coefficient
γ	phase change rate (s^{-1})
δ	thickness (m)
ε	porosity
$\zeta_{pt/c}$	platinum weight percentage of Pt/carbon catalyst
$\zeta_{im/c}$	mass ratio of ionomer to carbon
η	overpotential (V)
θ	correction coefficient
κ_{ele}	electronic conductivity (S m^{-1})
κ_{ion}	ionic conductivity (S m^{-1})
λ	membrane water content
μ	dynamic viscosity (kg m^{-1} s^{-1})
ρ	density (kg m^{-3})
σ	surface tension coefficient (N m^{-1})
φ_{ele}	electronic potential (V)
ω	energy parameter (J mol^{-1})

Subscripts and superscripts

0	standard state

1D	one-dimensional sub-model or domain
3D	three-dimensional sub-model or domain
ACL	anode catalyst layer
AEL	anode extra layer
a	anode
act	active
a/c	anode/cathode
ave	average
BP	bipolar plate
CL	catalyst layer
CCL	cathode catalyst layer
CEL	cathode extra layer
CL-MEM	interface of catalyst layer and membrane
c	cathode/carbon support
comp	air compressor
diff	diffusion
ECSA	electrochemically active surface area
EL	extra layer
EOD	electro-osmotic drag
eff	effective

ele	electronic
elch	electrochemical
eq	equilibrium
GDL	gas diffusion layer
GDL-MPL	interface of gas diffusion layer and micro-porous layer
g	gas mixture
g-im	gas-ionomer interface
hydr	hydraulic permeation
i	gas species
im	ionomer
im/c	ionomer/carbon
in	inlet
int	interface
ion	ionic
lw	liquid water
MEM	membrane
MPL	micro-porous layer
MPL-CL	interface of micro-porous layer and catalyst layer
m	mass
mesh	mesh

mw	membrane water
net	net
O_2	oxygen
out	output
pt	platinum
pt/im	platinum-ionomer coverage-dependent
pt/o	platinum-oxide coverage-dependent
pump	pump
ref	reference
rev	reversible
sat	local saturation state
T	temperature
total	total value
vp	water vapor
v-l	water vapor to liquid water
v-m	water vapor to membrane water
XL	lumped symbol of CL and MPL
ϕ	solving scalars in 1D domain
*	correction

1. Introduction

Proton exchange membrane (PEM) fuel cell has been widely acknowledged as one of the most promising energy conversion devices, especially for road transportation (e.g. fuel cell vehicles, FCVs). During the past decades, incredible achievements have been reached on not only cell performance but also stack manufacturing and hydrogen infrastructure [1], which propels the technology readiness of PEM fuel cell. However, there are still stringent requirements for the widespread commercialization of FCVs, such as higher power density (> 3 kW L^{-1}) and better durability (> 5000 h). In order to fulfill these targets, besides experimental efforts underway in the research community, modeling work also plays an important role in providing fast and in-depth support for technology development and helping avoid the huge cost of redundant experiments [2].

Plentiful models in a wide range of length scales have been developed, from atom to system [3, 4]. Some of them aim to shed light on mechanisms behind the sophisticated physicochemical phenomena occurring inside the PEM fuel cell, such as molecular dynamics (MD) [5], lattice Boltzmann method (LBM) [6], direct numerical simulation (DNS) [7], etc., which consider the real microscopic structure or even the molecular structure and are usually implemented in a very limited domain. Others pay more attention on the observable characteristics of cell performance and prefer to simulate the operation process in a complete fuel cell domain based on the continuum assumption. These models are often built up to provide some key information of PEM

fuel cell such as power output, distribution of reactants and products in certain operating conditions. They are often classified by the dimension of computational domain, namely one-dimensional (1D) [8, 9], two-dimensional (2D) [10, 11], three-dimensional (3D) [12] and combinations among them [13, 14]. Schumacher et al. [14] proposed a "2D+1D" model approach by coupling a two dimensional gas flow field plane with a point-to-point 1D membrane electrode assembly (MEA) model. The 2D field values are used as boundary conditions for 1D model and the fluxes of the 1D variables are returned as source terms in the 2D continuity equations. However, it is difficult for 2D description to follow the fast development of PEM fuel cell flow field. Evidence suggest that it is getting harder for traditional flow field (parallel, serpentine…) to meet the requirement of much higher power density (e.g. 6 kW L^{-1}) due to the bottleneck of gas supply. Flow fields with well-designed 3D structures have been proposed to break the limit, e.g. the 3D fine mesh flow field [15]. This has become a promising direction to further elevate the power density of PEM fuel cell, in cooperation with the development of catalyst activity. On the other hand, it is urgently needed for simulation tools to consider the full morphology of flow field layout and provide instructions and suggestions for those complex designs.

With all the dimensions taken into consideration, 3D model gives a more holistic view of cell operating state and yields better accuracy, also making higher requirement on computing resource. 3D model has been widely used to compare different flow field

designs and provide valuable guidance [16]. Single-channel or several-channel computational domains are often extracted in order to save calculation time [17]. For studies on flow field designs, active areas chosen in the open literature are mostly less than 50 cm^2 [16-19], which still remains a large gap compared with the size of commercial PEM fuel cell (~300 cm^2). Consequently, it is hard to reflect the function of the full flow field layout, especially for the distribution zone, which is usually neglected or simplified. As for large-scale simulation, 3D model is susceptible to long simulation time and unstable convergence [20]. For the sake of reducing the computational cost, Cordiner et al. [21] put forward a hierarchical 3D-1D approach that combined the 3D computational fluid dynamics (CFD) simulation of gas channel (GCH) and gas diffusion layer (GDL) with the 1D electrochemical description of catalyst layer (CL) and membrane (MEM). They simulated the coupling of different physical phenomena in PEM fuel cell and gained reasonable agreement with experimental data. Ding et al. [22] integrated the 3D volume of fluid (VOF) model with 1D MEA model in order to consider the impact of two-phase flow patterns in gas channel on the cell performance. Ferreira et al. [23] developed a similar "1D+3D" model and extended the single straight channel domain to the serpentine flow field with a GDL on the cathode side. The above "3D+1D" approach omitted a large portion of 3D domain girds and decoupled the fluid dynamics with electrochemical kinetics to some extent, thereby significantly saving the computational cost. In view of the real complicated structure, it is inevitable to simplify the MEA components when developing PEM fuel cell macro-

models and the difference lies in the degree of simplification. In fact, micro-porous layers (MPLs), CLs and MEM usually manifest as extremely thin slices with low permeability in typical 3D computational domains [24] and the transport process is mainly controlled by diffusion through the thickness direction (through-plane direction). For same reason, the precision of spatial discretization in these layers becomes very high and the grid density follows. From the perspective of macroscopic PEM fuel cell models, the "3D+1D" method can alleviate the heavy burden of mesh size and provide a potential way to find an optimal balance between computational cost and model accuracy, especially for large-scale simulation.

This study develops a "3D+1D" PEM fuel cell model by incorporating a 3D sub-model with a 1D sub-model. The 3D part runs the CFD simulation of GCH (or flow field) and GDL including both cathode and anode, together with an extra layer (EL) on each side which serves as the bridge establishing connections between the two sub-models. The 1D sub-model gives a comprehensive description of the simplified MEA components (MPLs, CLs, MEM) regarding mass and heat transfer, electrochemical reaction, agglomerate model of cathode CL, membrane water balance in both 3D part and 1D part of the model, which has not been attained in preceding studies to the best of the authors' knowledge. The main content of this paper includes an elaborate description of the proposed "3D+1D" modeling approach including a 3D sub-model and a 1D sub-model which are interrelated, followed by a detailed evaluation of the trade-off between

model accuracy and calculation efficiency in comparison with the whole 3D model. Then the model is adopted to investigate the partitioned optimization design on commonly-used PEM fuel cell flow field, and specifically, involving an active area of 345 cm^2 in keeping with the actual size of flow field for commercial application.

2. Model development

2.1 Model framework

Assumptions for the 3D sub-model:

Steady state; Laminar flow; Homogeneous porous media for GDLs and ELs; Mist-flow in gas channel.

Assumptions for the 1D sub-model:

One-dimensional transport; Fickian diffusion; Convection neglected; Homogeneous porous media for MPLs and CLs.

Fig. 1 shows the computational domain of the "3D+1D" model including the 3D domain (with geometry) and the 1D domain (no geometry). The 3D domain is comprised of bipolar plate (BP) (with gas channel, GCH) and gas diffusion layer (GDL) as well as an extra layer (EL) in both anode and cathode. Micro-porous layer (MPL), catalyst layer (CL) and membrane (MEM) are set as the 1D domain in connection with the extra layer via data exchange between the two sub-models. As schematized in Fig. 2, conservation equations are solved in the 3D domain and the scalar data stored in EL

grids provides boundary conditions for the 1D sub-model. Then source terms and physical parameters needed by 3D sub-model can be updated based on the 1D solutions. The 1D sub-model sets the computing nodes at the interfaces between MEA layers including the GDL-MPL interface, the MPL-CL interface and the CL-MEM interface on both anode and cathode sides as shown in the bottom right corner of Fig. 1. The scalar values of each layer are assumed to be arithmetic averages of the associated two interfaces. The ELs function as data storage library where mathematical manipulations and data updating take place in every iteration. In other words, the 1D sub-model runs in every grid of EL, which contains only one layer of mesh. It should be noted that the fluid zones of two sides are separated in the middle of anode EL (AEL) and cathode EL (CEL) but data exchanges between them. The "3D+1D" model is implemented on ANSYS FLUENT with the help of built-in transport equations and user-define function (UDF), through which the codes of 1D sub-model are implanted in.

2.2 Three-dimensional sub-model

The 3D sub-model solves the following conservation equations:

Mass (all fluid zones):

$$\frac{\partial}{\partial t}(\varepsilon(1-s)\rho_{\mathrm{g}}) + \nabla\cdot\left(\rho_{\mathrm{g}}\vec{u}_{\mathrm{g}}\right) = S_{\mathrm{m}} \tag{1}$$

Momentum (all fluid zones):

$$\frac{\partial}{\partial t}\left(\frac{\rho_{\mathrm{g}}\vec{u}_{\mathrm{g}}}{\varepsilon(1-s)}\right)+\nabla\cdot\left(\frac{\rho_{\mathrm{g}}\vec{u}_{\mathrm{g}}\vec{u}_{\mathrm{g}}}{\varepsilon^2(1-s)^2}\right)=-\nabla P_{\mathrm{g}}+$$
$$\mu_{\mathrm{g}}\nabla\cdot\left(\nabla\left(\frac{\vec{u}_{\mathrm{g}}}{\varepsilon(1-s)}\right)+\nabla\left(\frac{\vec{u}_{\mathrm{g}}^{\mathrm{T}}}{\varepsilon(1-s)}\right)\right)-\frac{2}{3}\mu_{\mathrm{g}}\nabla\cdot\left(\nabla\left(\frac{\vec{u}_{\mathrm{g}}}{\varepsilon(1-s)}\right)\right)+S_{\mathrm{u}} \quad (2)$$

Species (all fluid zones):

$$\frac{\partial}{\partial t}(\varepsilon(1-s)\rho_{\mathrm{g}}Y_{\mathrm{i}})+\nabla\cdot\left(\rho_{\mathrm{g}}\vec{u}_{\mathrm{g}}Y_{\mathrm{i}}\right)=\nabla\cdot(\rho_{\mathrm{g}}D_{\mathrm{i}}^{\mathrm{eff}}\nabla Y_{\mathrm{i}})+S_{\mathrm{i}} \quad (3)$$

Energy (all zones):

$$\frac{\partial}{\partial t}\left(\varepsilon s\rho_{\mathrm{lw}}C_{\mathrm{p,lw}}T+\varepsilon(1-s)\rho_{\mathrm{g}}C_{\mathrm{p,g}}T\right)+$$
$$\nabla\cdot\left(\varepsilon s\rho_{\mathrm{lw}}C_{\mathrm{p,lw}}\vec{u}_{\mathrm{lw}}T+\varepsilon(1-s)\rho_{\mathrm{g}}C_{\mathrm{p,g}}\vec{u}_{\mathrm{g}}T\right)=\nabla\cdot(k^{\mathrm{eff}}\nabla T)+S_{\mathrm{T}} \quad (4)$$

Liquid pressure (GDLs, ELs):

$$\frac{\partial}{\partial t}\left(\rho_{\mathrm{lw}}\varepsilon s\right)=\nabla\cdot\left(\rho_{\mathrm{lw}}\frac{Kk_{\mathrm{lw}}}{\mu_{\mathrm{lw}}}\nabla P_{\mathrm{lw}}\right)+S_{\mathrm{lw}} \quad (5)$$

Liquid water saturation (GCHs):

$$\frac{\partial}{\partial t}\left(\rho_{\mathrm{lw}}\varepsilon s\right)+\nabla\cdot\left(\rho_{\mathrm{lw}}\vec{u}_{\mathrm{lw}}s\right)=S_{\mathrm{lw}} \quad (6)$$

Electronic potential (BPs, GDLs and ELs):

$$0=\nabla\cdot\left(\kappa_{\mathrm{ele}}^{\mathrm{eff}}\nabla\varphi_{\mathrm{ele}}\right)+S_{\mathrm{ele}} \quad (7)$$

ε, ρ (kg m^{-3}), u (m s^{-1}), s, P (Pa), μ (kg m^{-1} s^{-1}), Y, D^{eff} (m^2 s^{-1}), C_{p} (J mol^{-1} K^{-1}), T (K), k^{eff} (W m^{-1} K^{-1}), K (m^2), k_{lw}, $\kappa_{\mathrm{ele}}^{\mathrm{eff}}$ (S m^{-1}) and φ_{ele} (V) are the porosity, the density, the superficial velocity, the liquid water saturation, the pressure, the viscosity, the species mass fraction, the effective gas diffusivity, the specific heat capacity, the temperature, the effective heat conductivity, the intrinsic permeability, the liquid phase relative permeability, the electronic conductivity and the electronic potential, respectively. S_{m} (kg m^{-3} s^{-1}), S_{u} (N m^{-3}), S_{i} (kg m^{-3} s^{-1}), S_{T} (W m^{-3}), S_{lw}

(kg m^{-3} s^{-1}) and S_{ele} (A m^{-3}) are corresponding source terms of the above equations. The subscripts "g", "lw" and "i" represent gas mixture, liquid water and gas species (hydrogen, oxygen and water vapor), respectively. Boundary conditions of GCH are set as mass-flow inlet and pressure outlet. The mass fluxes are calculated as below:

$$\begin{aligned} \dot{m}_{\mathrm{a}} &= \frac{j_{\mathrm{a}} ST_{\mathrm{a}} A_{\mathrm{act}}^{\mathrm{a}} \rho_{\mathrm{g}}^{\mathrm{a}}}{2FC_{\mathrm{H_2}}}\ ,\ C_{\mathrm{H_2}} = \frac{P_{\mathrm{g,in}}^{\mathrm{a}} - RH_{\mathrm{a}} P_{\mathrm{sat}}}{RT} \\ \dot{m}_{\mathrm{c}} &= \frac{j_{\mathrm{c}} ST_{\mathrm{c}} A_{\mathrm{act}}^{\mathrm{c}} \rho_{\mathrm{g}}^{\mathrm{c}}}{4FC_{\mathrm{O_2}}}\ ,\ C_{\mathrm{O_2}} = \frac{0.21\left(P_{\mathrm{g,in}}^{c} - RH_{\mathrm{c}} P_{\mathrm{sat}}\right)}{RT} \end{aligned} \tag{8}$$

where j (A m^{-3}), ST, A_{act} (m^2), RH and P_{sat} (Pa) are the electrochemical reaction rate in current form, the stoichiometric ratio, the active area, the inlet relative humidity and the water saturation pressure, respectively. As for the electronic potential equation, zero flux is set in the middle plane of two ELs and a reference potential is given on the other side. Constant temperature is specified to all the surrounding walls.

2.3 One-dimensional sub-model

Conservation equations of the 3D sub-model degenerates into flux equations in the 1D domain. For every computing node (i.e. one of the interfaces), the flux conservation equation can be built:

$$\sum J_{\phi} + \frac{S_{\phi}^{\mathrm{XL}} \delta_{\mathrm{XL}}}{2} + \frac{S_{\phi}^{\mathrm{YL}} \delta_{\mathrm{YL}}}{2} = 0 \tag{9}$$

where ϕ represents the solving scalars in 1D domain: species molar concentration (C_{i}), liquid pressure (P_{lw}), temperature (T), membrane water content (λ), electronic

potential (φ_{ele}) and ionic potential (φ_{ion}). J_ϕ (mol m^{-2} s^{-1}) and S_ϕ (mol m^{-3} s^{-1}) are the scalar fluxes and the source terms of corresponding MEA layers and δ (m) is the layer thickness. "XL" and "YL" are representative symbols of the two adjacent MEA layers as shown in Fig. 1 (GDLs, MPLs and CLs). The source terms of hydrogen and oxygen can be calculated from the electrochemical reaction rate:

$$S_{H_2}^{1D} = \frac{j_a}{2F},\ S_{O_2}^{1D} = \frac{j_c}{4F} \tag{10}$$

where j (A m^{-3}) and F (C mol^{-1}) are the reaction rate in current form and the Faraday constant. As for water transport, phase changes of water vapor into liquid water and membrane water are considered:

$$\begin{aligned} S_{vp}^{1D} &= \frac{j_c}{2F} - S_{v\text{-}m} - S_{v\text{-}l}^{1D} \\ S_{lw}^{1D} &= S_{v\text{-}l}^{1D} \\ S_{v\text{-}m}^{1D} &= \gamma_{v\text{-}m}(\lambda_{eq} - \lambda) \\ S_{v\text{-}l}^{1D} &= \begin{cases} \gamma_{v\text{-}l}\varepsilon(1-s)(C_{vp} - C_{sat}) & C_{vp} > C_{sat} \\ \gamma_{v\text{-}l}\varepsilon s(C_{vp} - C_{sat}) & C_{vp} < C_{sat} \end{cases} \end{aligned} \tag{11}$$

where γ (s^{-1}) and λ are the phase change rate and the membrane water content. Apart from the diffusion flux (diff), another two kinds of cross-membrane fluxes affect the transport of membrane water, namely the electro-osmotic drag flux (EOD) and the hydraulic permeation flux (hydr):

$$\begin{aligned} J_{diff} &= D_{mw}^{eff}\frac{\rho_{im}}{EW}\frac{\lambda_{int1} - \lambda_{int2}}{\delta_{MEM}} \\ J_{EOD} &= \frac{n_d I}{F} \\ J_{hydr} &= \frac{\rho_{lw} K_{MEM}}{M_{lw}\mu_{lw}}\frac{P_{lw,CCL} - P_{lw,ACL}}{\delta_{MEM}} \end{aligned} \tag{12}$$

where n_d, D_{mw} (m^2 s^{-1}), EW (kg mol^{-1}), and M (kg mol^{-1}) are the electro-osmotic drag coefficient, the membrane water diffusivity, the equivalent weight of dry ionomer, and the molecular weight, respectively. And the subscripts "int1" and "int2" represent two adjacent interfaces (MPL-CLs, CL-MEMs). The existence of liquid water in porous electrodes is described by liquid water saturation based on homogeneous porous media assumption, which can be obtained based on the solution of liquid pressure and Leveret-J function [25]:

$$\begin{aligned} P_c &= P_g - P_{lw} \\ P_c &= \sigma \cos\theta \left(\frac{\varepsilon}{K}\right)^{0.5} J(s) \\ J(s) &= \begin{cases} 1.417(1-s) - 2.12(1-s)^2 + 1.263(1-s)^3 & \theta < 90° \\ 1.417s - 2.12s^2 + 1.263s^3 & \theta > 90° \end{cases} \end{aligned} \tag{13}$$

where P_c (Pa), σ (N m^{-1}) and θ (°) are the capillary pressure, the surface tension coefficient and the contact angle of porous media. After getting the solution of water transport process, equilibrium membrane water content can be obtained:

$$\begin{aligned} \lambda_{eq} &= \begin{cases} 0.043 + 17.81a - 39.85a^2 + 36.0a^3 & 0 \leqslant a \leqslant 1 \\ 14.0 + 1.4(a-1) & 1 < a \leqslant 3 \end{cases} \\ a &= \frac{X_{vp} P_g}{P_{sat}} + 2s \end{aligned} \tag{14}$$

where a and X_{vp} are the water activity and the local mole fraction of water vapor. Then the ionic conductivity can be calculated with the solution of membrane water content:

$$\kappa_{ion} = (0.5139\lambda - 0.326) \exp\left[1268\left(\frac{1}{303.15} - \frac{1}{T}\right)\right] \tag{15}$$

The electrochemical overpotential can be obtained after solving the electronic potential

and the ionic potential:

$$\eta_{\text{elch}} = \varphi_{\text{ele}} - \varphi_{\text{ion}} \tag{16}$$

The boundary conditions of electronic potential in 1D domain is correlated with the solution of 3D domain:

$$\begin{aligned} \varphi_{\text{ele}}^{\text{AGDL-MPL}} &= E_{\text{rev}} - V_{\text{out}} - \varphi_{\text{ele}}^{\text{AEL}} \\ \varphi_{\text{ele}}^{\text{CGDL-MPL}} &= \varphi_{\text{ele}}^{\text{CEL}} \end{aligned} \tag{17}$$

where E_{rev} (V) and V_{out} (V) are the reversible potential and the output voltage, respectively. The former is usually derived by Nernst's equation and the latter depends on the cell operating condition.

$$E_{\text{rev}} = 1.229 + \frac{\Delta S}{2F}(T - T_{\text{ref}}) + \frac{RT}{2F}\left[\ln\left(\frac{P_{\text{H}_2,\text{a}}}{P_{\text{ref}}}\right) + \frac{1}{2}\ln\left(\frac{P_{\text{O}_2,\text{c}}}{P_{\text{ref}}}\right)\right] \tag{18}$$

where ΔS (J mol^{-1} K^{-1}) and R (J mol^{-1} K^{-1}) are the entropy change of the electrochemical reaction and the universal gas constant. The subscript "ref" represents reference state. With the electrochemical overpotential, the most important data in 1D sub-model —— the electrochemical reaction rate can be obtained using the Butler-Volmer (B-V) equation. The agglomerate model for cathode CL is also incorporated into the 1D sub-model and the B-V equation changed into the following form with the consideration of local transport resistance [26]:

$$\frac{C_{\text{O}_2}^{\text{g-im}} - C_{\text{O}_2}^{\text{pt}}}{R_{\text{local}}} = \frac{j_{\text{c}} A_{\text{im}}}{4F} \qquad j_{\text{c}} = k_{\text{elch}} \frac{C_{\text{O}_2}^{\text{pt}}}{C_{\text{O}_2}^{\text{ref}}} \tag{19}$$

$$j_{\text{c}} = \frac{RTC_{\text{O}_2}^{\text{CCL}}}{H_{\text{O}_2}} \left(\frac{C_{\text{O}_2}^{\text{ref}}}{k_{\text{elch}}} + \frac{R_{\text{local}}}{4FA_{\text{im}}}\right)^{-1} \tag{20}$$

$$k_{\mathrm{elch}} = i_{0,\mathrm{c}}^{\mathrm{ref}} A_{\mathrm{pt}}^{\mathrm{eff}} \theta_{\mathrm{T,c}} \left(1-\theta_{\mathrm{pt/o}}\right)\theta_{\mathrm{pt/im}} \left[\exp\left(\frac{4F\alpha_{\mathrm{c}}\eta_{\mathrm{elch,c}}}{RT} - \frac{\omega\theta_{\mathrm{pt/o}}}{RT}\right) - \exp\left(-\frac{4F(1-\alpha_{\mathrm{c}})\eta_{\mathrm{elch,c}}}{RT}\right)\right] \tag{21}$$

where i_0^{ref} (A m^{-2}), $A_{\mathrm{pt}}^{\mathrm{eff}}$ (m^{-1}), A_{im} (m^{-1}), R_{local} (s m^{-1}), k_{elch} (A m^{-3}), θ_{T}, $\theta_{\mathrm{pt/o}}$, $\theta_{\mathrm{pt/im}}$, H (Pa m^3 mol^{-1}), α and ω (J mol^{-1}) are the exchange current density, the effective specific platinum (Pt) area, the local transport resistance, the specific ionomer film area, the electrochemical coefficient, the temperature correction coefficient, the Pt-oxide coverage-dependent correction coefficient, the Pt-ionomer coverage-dependent correction coefficient, the Henry's constant, the transfer coefficient and the energy parameter. For the anode side, only the transport loss at gas-ionomer interface (using the Henry's constant) is considered due to much higher permeability of hydrogen:

$$j_{\mathrm{a}} = i_{0,\mathrm{a}}^{\mathrm{ref}} A_{\mathrm{pt}}^{\mathrm{eff}} \theta_{\mathrm{T,a}} \sqrt{\frac{RTC_{\mathrm{H_2}}^{\mathrm{ACL}}}{H_{\mathrm{H_2}} C_{\mathrm{H_2}}^{\mathrm{ref}}}} \left[\exp\left(\frac{2F\alpha_{\mathrm{a}}\eta_{\mathrm{elch,a}}}{RT}\right) - \exp\left(-\frac{2F(1-\alpha_{\mathrm{a}})\eta_{\mathrm{elch,a}}}{RT}\right)\right] \tag{22}$$

The specific Pt area can be calculated with electrochemical active surface area (ECSA) and Pt loading:

$$A_{\mathrm{pt}}^{\mathrm{eff}} = \frac{m_{\mathrm{pt}} a_{\mathrm{ECSA}}}{\delta_{\mathrm{CL}}} \tag{23}$$

where m_{pt} (g m^{-2}) and a_{ECSA} (m^2 g^{-1}) are the Pt loading and the ECSA, respectively. The source terms of charge potential equations can be obtained from the reaction rate:

$$S_{\mathrm{ele}}^{\mathrm{1D}} = \begin{cases} -j_{\mathrm{a}} \\ j_{\mathrm{c}} \end{cases} \qquad S_{\mathrm{ion}}^{\mathrm{1D}} = \begin{cases} j_{\mathrm{a}} & \mathrm{ACL} \\ -j_{\mathrm{c}} & \mathrm{CCL} \end{cases} \tag{24}$$

The heat source terms in the 1D domain takes different forms for different MEA layers:

$$S_{\mathrm{T}}^{\mathrm{1D}}=\begin{cases}\dfrac{I^2}{\kappa_{\mathrm{ele}}^{\mathrm{CL}}\varepsilon_{\mathrm{pt/c,ACL}}^{1.5}}+\dfrac{I^2}{\kappa_{\mathrm{ion}}\varepsilon_{\mathrm{im,ACL}}^{1.5}}+j_{\mathrm{a}}(\eta_{\mathrm{elch,a}}+\dfrac{T\Delta S_a}{4F})+hS_{\mathrm{v\text{-}l}} & \text{ACL}\\ \dfrac{I^2}{\kappa_{\mathrm{ele}}^{\mathrm{CL}}\varepsilon_{\mathrm{pt/c,CCL}}^{1.5}}+\dfrac{I^2}{\kappa_{\mathrm{ion}}\varepsilon_{\mathrm{im,CCL}}^{1.5}}+j_{\mathrm{c}}(-\eta_{\mathrm{elch,c}}+\dfrac{T\Delta S_c}{4F})+hS_{\mathrm{v\text{-}l}} & \text{CCL}\\ \dfrac{I^2}{\kappa_{\mathrm{ele}}^{\mathrm{MPL}}(1-\varepsilon_{\mathrm{MPL}})^{1.5}}+hS_{\mathrm{v\text{-}l}} & \text{MPLs}\\ \dfrac{I^2}{\kappa_{\mathrm{ion}}} & \text{MEM}\end{cases} \tag{25}$$

where h (J mol^{-1}) is the latent heat of water. And for other solving scalars (species molar concentration, liquid pressure and temperature), boundary conditions at GDL-MPL interfaces are given by values of EL grids:

$$\phi_{\mathrm{GDL\text{-}MPL}}=\phi_{\mathrm{EL}} \tag{26}$$

All the data stored in the extra layer and the information needed for 3D simulation can be updated in every iteration via the above equations. In order to guarantee the conservation of scalars, the source terms in 3D domain should be kept consistent with those in 1D domain through the following correlation:

$$S_{\phi}^{\mathrm{3D}}=\frac{J_{\phi}^{\mathrm{1D}}}{\delta_{\mathrm{EL}}} \tag{27}$$

Hence, the two sub-models are coupled together and the final solution can be obtained after an iterative solving process. The source terms for conservation equations in 3D sub-model are clarified in Table 1. And values and expressions of model parameters are listed in Table 2.

3. Results and discussion

3.1 Grid independency and model validation

The "3D+1D" model is firstly implemented in a single-channel PEM fuel cell domain as shown in Fig. 1 for grid independency test and model validation. Different maximum mesh sizes are tested at in-plane (IP) direction (X axis and Z axis) and through-plane (TP) direction (Y axis) as listed in Table 3. The average current density at 0.6 V output voltage is given as the criterion and mesh 7 is chosen for validation cases. Fig. 3 shows the comparison between the simulated polarization curves and the experimental data [27] under two cathode Pt loadings (0.2/0.1 mg cm^{-2}). And the simulation results of the whole 3D model (validated in the previous work [26]) are also given. Noting that the two models adopt the same parameter set. The maximum deviation of calculated current density is below 0.1 A cm^{-2}. Additionally, it can be seen that the polarization curves simulated by the two models are very close, which means both the "3D+1D" model and the 3D model have the ability to predict the fuel cell performance with acceptable accuracy. The comparison results forcefully prove the validity and feasibility of the "3D+1D" model.

3.2 Model accuracy and calculation efficiency

To further evaluate the application potential of the proposed "3D+1D" approach, the comparison of the two models is extended to a larger PEM fuel cell with an active area of 345 cm^2 as shown in Fig. 4 and the parallel-serpentine (PS) flow field design is

applied on both anode and cathode sides. Fig. 5 compares the detailed distribution of oxygen molar concentration (middle plane of cathode GDL at TP direction), cathode electrochemical overpotential and membrane water content at 0.6V output voltage. The contours of the 3D model results are extracted from the middle plane of the corresponding layers. For the "3D+1D" model, the cathode electrochemical overpotential and membrane water content can be drawn by depicting the data stored in the cathode extra layer. Similar distribution patterns can be found for all the three contours, which supports the feasibility of "3D+1D" method again. The average current density turns out to be a little higher (2.0A cm^{-2} vs. 1.7A cm^{-2}) due to slightly larger values of ovepotential and membrane water content calculated by "3D+1D" model. This is probably because of the simplification of in-plane transport process in MEA layers.

Moreover, this study also focuses on another important factor: the time cost of simulation. In consideration of larger GCH cross section size and limited computing resource, the grid density of mesh 1 is adopted for 345 cm^2 cases. The mesh quantity and simulation time of the comparison cases as well as the hardware configuration of the computing platform are given in Table 4. It can be seen that the calculation time of the "3D+1D" model is about 20 folds shorter than the whole 3D model for the same flow field domain. One of the main reasons for the boost of calculation efficiency is the decrease of mesh quantity. As mentioned before, the thin MEA layers (MPLs, CLs,

MEM) make high demand on grid density, which brings considerable burden on calculation speed. Another important reason roots in the simplification of transport dimension. The flow conservation equations (mass, momentum) are neglected in 1D domain and others degenerates into flux equations. Generally speaking, "3D+1D" model gives a decent trade-off between model accuracy and calculation efficiency and provides an efficient tool for large-scale simulation studies, especially for those on PEM fuel cell flow field.

3.3 Flow field design investigation

It has been difficult for the cathode side of PEM fuel cell to elegantly overcome the risk of gas starvation and water flooding, which pins high expectation on the cathode flow field. As for commercial application scenario, two kinds of flow field are often adopted or based on for PEM fuel cell, parallel design and parallel-serpentine design. And the parallel flow field is usually combined with some improvements in the distribution zone like adding dots or slots [28, 29], aiming for more uniform gas distribution. In this section, three cathode flow field designs are compared on a large-scale PEM fuel cell with 345 cm^2 active area by using the established "3D+1D" model, namely the parallel-serpentine design (PS), the parallel design with dots (PD) and the parallel design with dots and waves (PDW). As shown in Fig. 6, traditional straight channel and wavy channel (proposed by Honda [30]) are combined to enhance the gas convection without adding too much flow resistance. All the anode sides use the PS flow field and the

reverse-flow arrangement is adopted throughout the simulation in this paper. The geometry information of single-channel cell domain and the 345 cm^{-2} cell domain is given in Table 5. The back total pressure of all the cases are set as 1.5 atm.

Fig. 7 shows the comparison of pressure drop, polarization curve and net power density among the three cathode flow field designs under high inlet humidity ($RH_{a/c}$ 1.0/1.0) and stoichiometric ratio ($ST_{a/c}$ 1.5/2.0). The parasitic pumping loss can be derived from the pressure drop:

$$W_{net} = W - W_{pump}, \quad W_{pump} = \frac{\Delta P \overline{u_{in}} A_{in}}{A_{act} \eta_{comp}} \tag{28}$$

where W (W m^{-2}), ΔP (Pa), $\overline{u_{in}}$ (m s^{-1}), A_{in} (m^2), A_{act} (m^2) and η_{comp} are the power density, the pressure drop, the average inlet velocity, the inlet area, the active area and the air compressor efficiency (70% is adopted). It can be seen from Fig. 7a that the pressure drop of the PDW design does not increase distinctly compared with the PD design because of larger width of wavy channel and the PS design yields the highest flow resistance. Under higher inlet humidification and stoichiometric ratio, the cell performance of the PS design and the PD design has no obvious difference while the PDW design gives slightly higher power density around 0.4 V output voltage (see Fig. 7b). This is possibly because that the wavy structure improves the gas distribution by enhancing the cross-flow convection. Then dryer inlet condition ($RH_{a/c}$ 0.4/0.2) and lower stoichiometric ratio ($ST_{a/c}$ 1.2/1.6) are further tested as shown in Fig. 8, the PDW

design performs much better than the other two designs and the polarization curve shows different trend in high current region. In this case, besides the reason on reactant gas supply, the water retention effect of the wavy structure is also significant.

As displayed in Fig. 9, contours of the oxygen molar concentration and the liquid water saturation at the middle plane of cathode GDL are compared under the aforementioned two operating conditions. It can be seen from Fig. 9a that the PDW design provides the most uniform oxygen distribution and the addition of wavy channel alleviates the local gas starvation under both two stoichiometric ratios, as contrasted with the results of the PD design. And the liquid water is prone to accumulate under the wavy structure probably due to the difficulty of gas flow, which may cause flooding when the inlet gas is fully humidified. However, the water retention effect turns to be beneficial for cell operation under low inlet relative humidity and contributes to the so-called self-humidification mechanism, which has become a common pursuit for PEM fuel cell application [31]. For the PDW design, the liquid water blocked by the wavy structure improves the membrane hydration and increases the ionic conductivity, which explains the upwarp of polarization curve under high current density. In terms of water removal, the flow resistance is much higher in the wavy channels due to the bending structure and the retained water and the difference of gas velocity (also pressure difference) forms between the wavy channels and straight channels. As a result, the redundant water can be removed through the straight channel forming a water transport path as shown in Fig.

9b, which can reduce the risk of water flooding. Though the maximum net power density of the three flow field designs gains little difference, the PDW design shows excellent stability of power output in high current region and can attain better membrane hydration under extremely low external humidification. Overall, the proposed parallel flow field with dots and waves is suitable for application scenario under low humidification and high current density, which is highly expected for future PEM fuel cells without external humidifier. The above simulation work proves the feasibility of partitioned optimization design for PEM fuel cell flow field and also the necessity of adopting "3D+1D" modeling method for large-scale simulation, when the full morphology of flow field layout is concerned. In addition, computing methods relating to the artificial intelligence (AI) like big data and machine learning are currently regarded as novel approach to help with the mathematical modeling work on energy research field [32]. The "3D+1D" model is expected to provide large-scale simulation data for the data-driven PEM fuel cell models [33] in consideration of the advantage on calculation speed.

4. Conclusion

In this study, a "3D+1D" PEM fuel cell model aiming for large-scale simulation is developed, which consists of two interrelated sub-models (3D and 1D). The computational domain also contains 3D part (bipolar plate, gas channel and gas diffusion layer) and 1D part (micro-porous layer, catalyst layer and membrane). The

former has geometry and mesh while the latter is embedded into the girds of extra layers in the 3D domain, which serve as a bridge connecting the two sub-models. Conservation equations are solved by the 3D sub-model and the 1D sub-model obtains solutions using the data from 3D grids and updates parameters for subsequent iterations. Reasonable agreement between simulation results and experimental data is attained. And by further comparing the "3D+1D" model with the whole 3D model, the trade-off between model accuracy calculation efficiency and is evaluated, involving both the single-channel domain and the whole-cell domain with 345 cm^2 active area. Using the "3D+1D" model, the commonly-used two flow field designs, the parallel-serpentine flow field (PS) and the parallel flow field with dots in distribution zone (PD) together with a partitioned design adding wavy channel to the PD design (PDW) are simulated on the 345 cm^2 cell domain. The main conclusions are drawn as below:

- The calculation efficiency is found to be greatly promoted adopting the "3D+1D" modeling approach in comparison with the whole 3D model. The simulation time is shortened by 20 folds for the 345 cm^2 cell domain cases in this study. The main reasons includes the decrease of mesh quantity and the reasonable simplification of transport dimension. And the "3D+1D" model also gains decent accuracy, which is supported by the similar simulation results from the two models.
- The proposed combinational flow field design with dots in the distribution zone and waves in the straight-flow zone (the PDW design) yields better cell performance than the PS design and the PD design without increasing much

pressure drop. And owing to the cross-flow convection enhancement and water retention effect of wavy structure, the PDW design shows excellent adaptability under low inlet humidification and stoichiometric ratio, which also has become a promising trend for the development of PEM fuel cell. Considering the manufacturing possibility and convenience, the partitioned flow field designs could be still based on the rib/channel structure and take advantage of the current technology.

- In general, the partitioned optimization design (PDW) provides a feasible and potential way to develop the next-generation PEM fuel cell flow field and stresses the importance to consider the full morphology of flow field layout. The "3D+1D" model is expected to play an irreplaceable role in large-scale or commercial-scale simulation regarding the studies on a complete PEM fuel cell or even a small stack, as a powerful and efficient tool.

This study is expected to help address the urgent need of large-scale simulation ability in the R&D of PEM fuel cell vehicles for road transportation. The assumptions of the current "3D+1D" model still remains inappropriateness (e.g. mist-flow in gas channel) and the model validation should be extended to large-scale experimental data. The following study will focus on the further validation of the "3D+1D" modeling method and the correction on the solution of liquid water saturation in flow channel with the help of VOF model and experimental visualization.

Acknowledgements

This work is supported by the National Key Research and Development Program of China (Grant No. 2016YFB0101303) and the National Natural Science Foundation of Tianjin (China) for Distinguished Young Scholars (Grant No. 18JCJQJC46700). We also thank for the support of Shanghai H-Rise New Energy Technology Co. Ltd., China FAW Group Co. Ltd. and Shanghai Hydrogen Propulsion Technology Co. Ltd.

References

[1] Wang Y, Chen K, Mishler J, Cho S, Adroher X. A review of polymer electrolyte membrane fuel cells: Technology, applications, and needs on fundamental research. Applied Energy, 88 (4) (2011), 981-1007.

[2] Wu H. A review of recent development: Transport and performance modeling of PEM fuel cells. Applied Energy, 165 (2016), 81-106.

[3] Jahnke T, Futter N, Latz A, et al. Performance and degradation of Proton Exchange Membrane Fuel Cells: State of the art in modeling from atomistic to system scale. The Journal of Physical Chemistry Letters. 10 (20) (2019), 6409-6413.

[4] Qi Y, Espinoza-Andlauz M, Thern M, Andersson M. Polymer electrolyte fuel cell system level modelling and simulation of transient behavior. eTransportation, 2 (2019), 100030.

[5] Fan L, Wu K, Tongsh X, Zhu M, Xie X, Jiao K. Mechanism of Water Content on the Electrochemical Surface Area of the Catalyst Layer in the Proton Exchange

Membrane Fuel Cell. Journal of Power Sources, 143 (1-2) (2005), 103-124.

[6] Kim K, Kang J, Lee S, Nam J, Kim C. Lattice Boltzmann simulation of liquid water transport in microporous and gas diffusion layers of polymer electrolyte membrane fuel cells. 278 (2015), 703-717.

[7] Wang G, Mukherjee P, Wang C Y. Optimization of polymer electrolyte fuel cell cathode catalyst layers via direct numerical simulation modeling. Electrochimica Acta, 52 (22) (2003), 6367-6377.

[8] Ju H, Meng H, Wang C Y. A single-phase, non-isothermal model for PEM fuel cells. International Journal of Heat and Mass Transfer, 48(7) (2005), 1303-1315.

[9] Rahman M, Mojika F, Sarker M, Chuang P. Development of 1-D multiphysics PEMFC model with dry limiting current experimental validation. Electrochimica Acta, 320 (10) (2019), 134601.

[10] Liu J, Guo H, Ye F, Ma C. Two-dimensional analytical model of a proton exchange membrane fuel cell. Energy, 119 (2017), 299-308.

[11] Robin C, Gerard M, Arbigny J, Schott P, Jabbour L, Bultel Y. Development and experimental validation of a PEM fuel cell 2D-model to study heterogeneities effects along large-area cell surface. International Journal of Hydrogen Energy, 40 (32) (2015), 10211-10230.

[12] Baca C, Travis R, Bang M, Djilali N. Three-dimensional, single-phase, non-isothermal CFD model of a PEM fuel cell. Journal of Power Sources, 178 (1) (2008), 269-281.

[13] Kulikovsky A. Semi-analytical 1D + 1D model of a polymer electrolyte fuel cell. Electrochemistry Communications, 6 (10) (2004), 969-977.

[14] Schumacher J, Eller J, Sartoris G, Colinart T, Seyfang B. 2+1D modelling of a polymer electrolyte fuel cell with glassy-carbon microstructures. Mathematical and Computer Modelling of Dynamical Systems, 18 (4) (2012), 355-377.

[15] Yoshida T, Kojima K. Toyota MIRAI fuel cell vehicle and progress toward a future hydrogen society. Electrochemical Society Interface, 24 (2) (2015), 45-49.

[16] Chiu H C, Jang J H, Yan W M, Li H Y, Liao C C. A three-dimensional modeling of transport phenomena of proton exchange membrane fuel cells with various flow fields. Applied Energy, 96 (2012), 359-370.

[17] Wu H, Berg P, Li X. Steady and unsteady 3D non-isothermal modeling of PEM fuel cells with the effect of non-equilibrium phase transfer. Applied Energy, 87 (9) (2010), 2778-2784.

[18] Carton J, Olabi A. Three-dimensional proton exchange membrane fuel cell model: Comparison of double channel and open pore cellular foam flow plates. Energy, 136 (2017), 185-195.

[19] Vazifeshenas Y, Sedighi K. Numerical investigation of a novel compound flow-field for PEMFC performance improvement. International Journal of Hydrogen Energy, 40 (43) (2015), 15032-15039.

[20] Falcao D, Gomes P, Oliveira V, Pinho C, Pinto A. 1D and 3D numerical simulations in PEM fuel cells. International Journal of Hydrogen Energy, 36 (19) (2011),

12486-12498

[21] Cordiner S, Mulone V, Romanelli F. Thermal-Fluid-Dynamic Simulation of a Proton Exchange Membrane Fuel Cell Using a Hierarchical 3D-1D Approach. Journal of Electrochemical Energy Conversion and Storage, 4 (3) (2007), 317-327.

[22] Ding Y, Bi X, Wilkinson D. 3D simulations of the impact of two-phase flow on PEM fuel cell performance. Chemical Engineering Science, 100 (2013), 445-455.

[23] Ferreira R, Falcao D, Oliveira V, Pinto A. 1D + 3D two-phase flow numerical model of a proton exchange membrane fuel cell. Applied Energy, 203 (2017), 474-495.

[24] Li W, Zhang Q, Wang C, Yan X, Shen S, Xia G, Zhu F, Zhang J. Experimental and numerical analysis of a three-dimensional flow field for PEMFCs. Applied Energy, 195 (2017), 278-288.

[25] Zhang G, Fan L, Sun J, Jiao K. A 3D model of PEMFC considering detailed multiphase flow and anisotropic transport properties. International Journal of Heat and Mass Transfer, 115 (2017), 714-724.

[26] Xie B, Zhang G, Xuan J, Jiao K. Three-dimensional multi-phase model of PEM fuel cell coupled with improved agglomerate sub-model of catalyst layer. Energy Conversion and Management, 199 (2019), 112051.

[27] Owejan J P, Owejan J E, Gu W. Impact of Platinum Loading and Catalyst Layer Structure on PEMFC Performance. Journal of The Electrochemical Society, 160 (8) (2013), F824-F833.

[28] Zhang G, Xie X, Xie B, Du Q, Jiao K. Large-scale multi-phase simulation of proton exchange membrane fuel cell. International Journal of Heat and Mass Transfer, 130 (2019), 555-563.

[29] Song Y, Zhang C, Ling C Y, et al. Review on current research of materials, fabrication and application for bipolar plate in proton exchange membrane fuel cell. International Journal of Hydrogen Energy, (2019). https://doi.org/10.1016/j.ijhydene.2019.07.231

[30] Tanaka S, Nagumo K, Yamamoto M, Chiba H, Yoshida K, Okano R. Fuel cell system for Honda CLARITY fuel cell. eTransportation, 3 (2020), 100046.

[31] Martin S, Garcia-Ybarra P, Castillo J. Long-term operation of a proton exchange membrane fuel cell without external humidification. Applied Energy, 205 (2017), 1012-1020.

[32] Bejan A. AI and freedom for evolution in energy science. Energy and AI, 1 (2020), 100001.

[33] Wang B, Zhang G, Wang H, Xuan J, Jiao K. Multi-physics-resolved digital twin of proton exchange membrane fuel cells with a data-driven surrogate model. Energy and AI, 1 (2020), 100004.

Figure and table captions

Fig. 1. Computational domain of the “3D+1D” model including the 3D domain (with geometry) and the 1D domain (no geometry).

Fig. 2. Solution flowchart of the "3D+1D" model in every iteration.

Fig. 3. Comparison between simulated polarization curves by the "3D+1D" model and experimental data under two cathode Pt loadings [27]. The preceding simulation results of 3D model [26] are also given. Operating conditions (anode/cathode): inlet relative humidity (1.0/1.0), stoichiometric ratio (3.0/4.0), back total pressure (1.5/1.5 atm), operating temperature (353.15 K).

Fig. 4. Schematic of the large-scale computational domain with 345 cm^2 active area.

Fig. 5. Comparison of oxygen molar concentration, cathode electrochemical overpotential and membrane water content between the 3D model and the "3D+1D" model at the 0.6 V output voltage data point.

Fig. 6. Schematic of the three different flow field designs (PS, PD, PDW).

Fig. 7. Comparison of (a) pressure drop; (b) polarization curve and net power density among the three cathode flow field designs under high inlet humidity ($RH_{a/c}$ 1.0/1.0) and stoichiometric ratio ($ST_{a/c}$ 1.5/2.0).

Fig. 8. Comparison of polarization curve and net power density among the three cathode flow field designs under low inlet humidity ($RH_{a/c}$ 0.4/0.2) and stoichiometric ratio ($ST_{a/c}$ 1.2/1.6).

Fig. 9. Comparison of (a) oxygen molar concentration contour; (b) liquid water saturation contour in the middle plane of cathode GDL among the three flow field designs.

Table 1. Source terms of 3D sub-model.

Table 2. Values and expressions of model parameters.

Table 3. Grid independency test results.

Table 4. Mesh quantity and simulation time of the comparison cases.

Table 5. Geometry information of the computational domains.